Geofísica Internacional (2026) **65-2**: 2071- 2088

Application of geophysical and hydrogeochemical methods in the Zimapán Aquifer, Hidalgo for environmental purposes

Tania Karen Espinoza-Juárez[1], José Iván Morales-Arredondo[2], María Aurora Armienta Hernández[2], Ana Caccavari-Garza[3], Gerardo Cifuentes Nava[3], Daniel Armando Pérez-Calderón[4], Abigail Mosso-Mendoza[5]

Abstract

The region of Zimapán, Hidalgo, situated within the Tolimán watershed, faces groundwater contamination issues due to high concentrations of arsenic (As) and, in certain sites, fluoride (F^-). This pollution is associated with the presence of several mineral deposits enriched with metallic sulfides, such as pyrite and arsenopyrite, as well as other minerals such as scorodite, a mineral produced by an exothermic process that releases sulfate. The origin of this mineralization stems from two distinct mineralization events: the initial event, linked with intrusions, and the subsequent event, characterized as hydrothermal in nature. These post-tectonic events, together with the Laramide orogeny, have generated an abrupt geomorphology and deformation, mainly in the carbonate sequence, which is covered by volcanic sediments. This makes it difficult to characterize geological structures that are continuous at depth and that may influence the aquifer system and the contamination of the basin.

This study aims to identify and analyze the geological formations potentially associated with the occurrence of arsenic in groundwater at specific locations that influence groundwater dynamics, as well as structural formations that act as sources and pathways for the transport of these solutes. In pursuit of this objective, various methods were employed to regionally characterize and infer subsurface structures. Magnetic anomaly and Bouguer anomaly data were utilized. Utilizing this information, indirect 3D three-dimensional models of the study area were constructed, which were linked to the geological formations prevalent in the area through a thorough analysis of gravimetric and aeromagnetic anomalies.

Among the most relevant results obtained, we observed the presence of highly dense bodies associated with granitic intrusions. Additionally, certain lineaments were identified that align with NW-SE geological faults validated in previous works with other methodologies, which link the mineralization resulting from the granitic intrusions and enrich groundwater with highly toxic metals and metalloids, mainly with arsenic.

Finally, hydrogeochemistry proved to be useful in evaluating the influence relationship between the main anomalous bodies and natural groundwater contamination.

Key words: Arsenic, hydrogeochemistry, geophysics, contamination, aquifer.

Resumen

La región de Zimapán, Hidalgo, ubicada en la cuenca hidrográfica del Tolimán, enfrenta problemas de contaminación en el agua subterránea por elevadas concentraciones de arsénico (As) y en algunos casos de fluoruros (F^-). Esta contaminación se asocia a la presencia de varios depósitos minerales enriquecidos con sulfuros metálicos, como pirita y arsenopirita, así como otros minerales como la escorodita, mineral producto de un proceso exotérmico que libera sulfato. El origen de esta mineralización se debe a dos eventos principales: el primero, asociado con intrusiones, y el segundo, de tipo hidrotermal. Estos eventos postectónicos en conjunto con la orogénesis laramídica han generado una abrupta geomorfología y deformación principalmente en la secuencia carbonatada, que está recubierta por sedimentos volcánicos, motivo por el cual resulta complicado caracterizar estructuras geológicas que tienen continuidad a profundidad y que pueden influir en el sistema acuífero y la contaminación de la cuenca.

El objetivo de este trabajo fue localizar y caracterizar las formaciones geológicas que pudieran estar relacionadas con la presencia de As en el agua subterránea de algunos sitios que controlan la dinámica del acuífero, así como formaciones estructurales que sirven como fuente y conducto del transporte de estos solutos. Para ello, se emplearon métodos potenciales con el fin de caracterizar regionalmente e inferir estructuras a profundidad; se emplearon datos de anomalía magnética y anomalía de Bouguer. Con esta información se elaboraron modelos indirectos 3D de la zona de estudio, que con base en el análisis integral de las anomalías gravimétricas y aeromagnéticas se asociaron con las formaciones geológicas que predominan en la zona.

Entre los resultados obtenidos más relevantes, se encontró la presencia de cuerpos altamente densos, que se asocian a intrusiones graníticas. También, se identificaron algunos lineamientos que coinciden con fallas geológicas NW-SE reportadas en trabajos previos con otras metodologías, las cuales interconectan la mineralización originada por las intrusiones graníticas y pueden enriquecer el agua subterránea con metales y metaloides altamente tóxicos como es el caso del arsénico.

Finalmente, la hidrogeoquímica permitió evaluar la relación entre los cuerpos anómalos principales y la contaminación natural del agua subterránea.

Palabras clave: Arsénico, hidrogeoquímica, geofísica, contaminación, acuífero.

Received: September 19, 2025; Accepted: February 26, 2026; Published on-line: April 1, 2026.

Editorial responsibility: Dr. Fernando Corbo-Camargo

* Corresponding author: José Iván Morales - Arredondo, ivanma@igeofisica.unam.mx
[1] Universidad Nacional Autónoma de México, Posgrado en Ciencias de la Tierra, Coyoacán, 04150, CDMX
[2] Universidad Nacional Autónoma de México, Instituto de Geofísica, Departamento de Recursos Naturales, Coyoacán, 04150, CDMX.
[3] Universidad Nacional Autónoma de México, Instituto de Geofísica, Servicio Magnético, Coyoacán, 04150, CDMX.
[4] Universidad Nacional Autónoma de México, Instituto de Geofísica, Departamento de Geomagnetismo y Exploración, Coyoacán, 04150, CDMX.
[5] Universidad Nacional Autónoma de México, Escuela Nacional en Ciencias de la Tierra, Coyoacán, 04150, CDMX.

Tania Karen Espinoza-Juárez, Iván Morales-Arredondo, María Aurora Armienta-Hernández, Ana Caccavari-Garza, Gerardo Cifuentes Nava, Daniel Armando Pérez-Calderón and Abigail Mosso-Mendoza

https://doi.org/10.22201/igeof.2954436xe.2026.65.2.1916

1. Introduction

During the last decade, arsenic (As) contamination has been identified in groundwater of various regions of the world. The highest levels of As have been determined in Asia and Europe, followed by Africa, North America, South America, and Australia (Shaji *et al.*, 2021). This metalloid is widely known due to its extensive use in science, medicine, and technology, as well as its toxicity (Armienta *et al.*, 1995). Since its health risk includes both carcinogenic and non-carcinogenic effects (Singh *et al.*, 2021), the World Health Organization (WHO) establishes that the permissible limit for arsenic in drinking water is 0.01 mg/L (World Health Organization, 2011; Jha *et al.*, 2023). The presence of arsenic in Mexico has been known since the 1960s, with various health effects reported in the Comarca Lagunera region of northern Mexico (Cebrian *et al.*, 1983; Armienta *et al.*, 2008).

Therefore, NOM-127-SSA1-2021, is the Mexican Standard for Water for Human Use and Consumption, which defines the permissible limit for arsenic in drinking water as 0.025 mg/L for all localities and will be adjusted according to the gradual compliance schedule, until reaching a maximum value of 0.01 mg/L (Secretaría de Salud, 2022).

Since 1992, high concentrations of arsenic have been detected in the water sourced from drinking water wells in the municipality of Zimapán, posing an environmental hazard. Armienta *et al.* (1997a; 2001) based on hydrogeological, hydrogeochemical, mineralogical and chemical determinations (rocks, tailings, soils) and geological studies identified three primary sources of contamination in the aquifer system:

a) Natural from water interaction with mineralized limestone rock and iron oxides/hydroxides in the deep fractured limestone aquifer, with arsenic concentrations exceeding 1.09 mg/L
b) Mine tailings releasing arsenic up to 0.437 mg/L to the shallow aquifer.
c) Arsenic-laden vapors that permeated the soil, producing water concentrations of 0.10 mg/L in shallow wells.

Arsenic contamination is associated with mineral deposits enriched in metallic sulfides such as pyrite and arsenopyrite, as well as minerals like scorodite. Arsenic release into groundwater is mainly driven by arsenopyrite oxidation near mineralized zones, an exothermic process that lowers pH and increases sulfate and temperature, releasing arsenic into the water (Dove & Rimstidt,

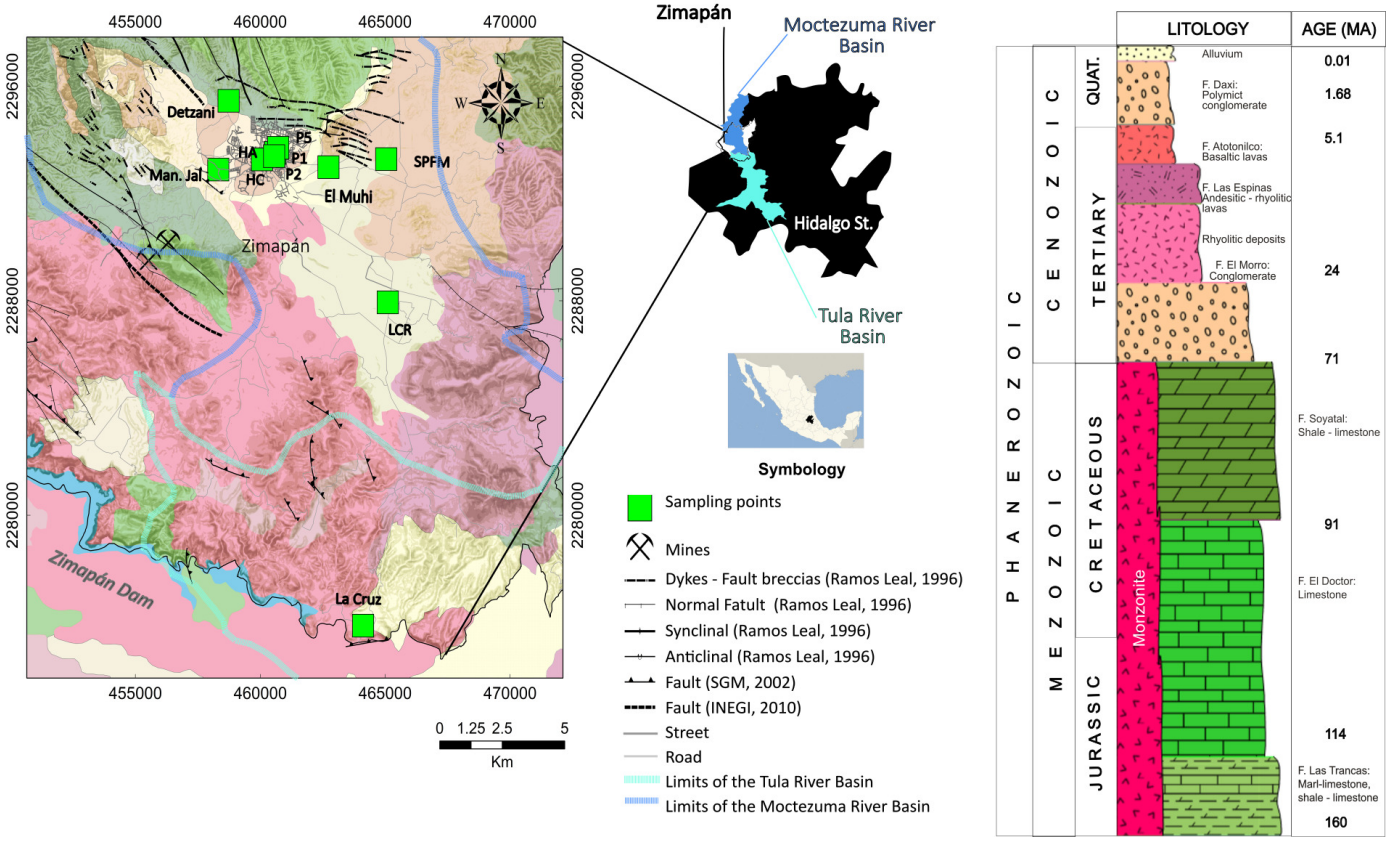


Figure 1. Lithology and structural geology of Zimapán, Hidalgo (Derived and modified from INEGI, 2002, 2010; Servicio Geológico Mexicano, 2002; Ramos Leal, 1996).

1985; Armienta *et al.*, 2001). Evidence of oxidation observed in cave rocks, which show high arsenic concentrations, together with water–rock geochemistry, supports this mechanism. Arsenic transport occurs predominantly through fractures in Cretaceous limestones (Tamaulipas or Soyatal Formation) (Armienta *et al.*, 2001), while the presence of scorodite suggests that its precipitation at low pH followed by incongruent dissolution may also contribute to arsenic in groundwater.

Anthropogenic and natural sources of arsenic in Zimapán have been confirmed based also on groundwater isotopic determinations. Point sources are linked to mining activities contaminating shallow wells located near tailings or former smelters, and diffuse sources are linked to regional flow systems in carbonate rocks with presence of arsenic minerals and iron oxides/hydroxides releasing As to the deep wells (Sracek *et al.*, 2010), remarking that the diffuse source has significantly affected the health of the population in Zimapán due to the consumption of water from the deep aquifer (Armienta *et al.*, 1997b; Del Razo *et al.*, 2011).

In this context, a geophysical model of the study area was developed by analyzing the natural responses of the magnetic and Bouguer anomalies to deduce subsurface structures and lineaments that are challenging to detect through alternative methods, thereby elucidating the relationship between geological structures and groundwater chemistry, focused on arsenic occurrence.

Given that geology (Figure 1) can be significantly affected by faults, fractures, folds, and thrusts, the gravimetric method is ideal for identifying these structures, as it relies on measuring the Earth's gravitational field to characterize subsurface features based on the density, to locate deep contacts, and determine their lateral and vertical extents (Toushmalani, 2010).

The magnetic method facilitates the identification of changes in magnetic susceptibility related to changes in lithology, stratigraphic unit thickness, or the distribution of specific minerals that may influence groundwater chemistry (Dentith & Mudge, 2014); filters and corrections are employed to emphasize particular characteristics of the anomalies (Baranov & Naudy, 1964; López-Loera & Tristán-González, 2013; Milligan & Gunn, 1997; Fanton *et al.*, 2014).

While geophysical methods alone offer enhanced insights into structural geology and lithology, this data can be integrated with chemical analyses to improve comprehension of groundwater quality in the aquifer (Gómez-Hernández *et al.*, 2020; Alabi *et al.*, 2020; Song *et al.*, 2020; Eyankware *et al.*, 2021). Electrical resistivity investigations are typically conducted alongside hydrogeochemical data for integrated analysis aimed at assessing groundwater quality, contamination and risk (Ismail *et al.*, 2022). At the regional level, potential field methods facilitate the identification of anomalies and the assessment of the depths, geometry, and distribution of geological bodies that may influence the hydrogeochemistry (Andres Sanchez & Sanchez San Roman, 1998; Telford *et al.*, 1990; Hsu *et al.*, 1996; Rankin & Triggs, 1997).

2. Location

The study area involves the Zimapán aquifer system, which is located within two main hydrological basins: the Moctezuma River basin and the Tula River basin, both belonging to the Pánuco hydrological region (CONAGUA, 2021). Zimapán, the municipality that encompasses both basins, is in the state of Hidalgo, between 20° 34' and 20° 58' north latitude and 99° 11' and 99° 33' west longitude. Its altitude ranges from 900 to 2,900 meters, covering an area of 720 km² (INEGI, 2010). The predominant physiographic provinces in the area are the Sierra Madre Oriental and the Trans-Mexican Volcanic Belt (Figure 2), which serve as watersheds and recharging zones for the Zimapán aquifer system within the basins delimited by the Tolimán stream, an effluent of the Río Moctezuma (CONAGUA, 2021).

3. Geology

3.1. Stratigraphy

Mezozoic

Upper Jurassic

It consists of a sequence of limonites and shales corresponding to the Las Trancas Formation (Mora, 1998; Martínez Flores & Ortega Gamboa, 2009).

Lower Cretaceous

The El Doctor Formation, or Tamaulipas Formation, comprises a sequence of massive batholithic and reefal limestone rocks banded with flint nodules.

Upper Cretaceous

The Soyatal Formation, dating from this period, overlies the El Doctor Formation and comprises flysch deposits characterized by an intercalation of calcareous shales, sandstones, limonites, and limestones (Mora, 1998; Martínez Flores & Ortega Gamboa, 2009; Simons & Mapes, 1956), however, shales become predominant towards the upper strata (Simons & Mapes, 1956).

Cenozoic

Paleogene

The El Morro Formation is the predominant one in this age, encompassing the entire Eocene epoch and the lower portion

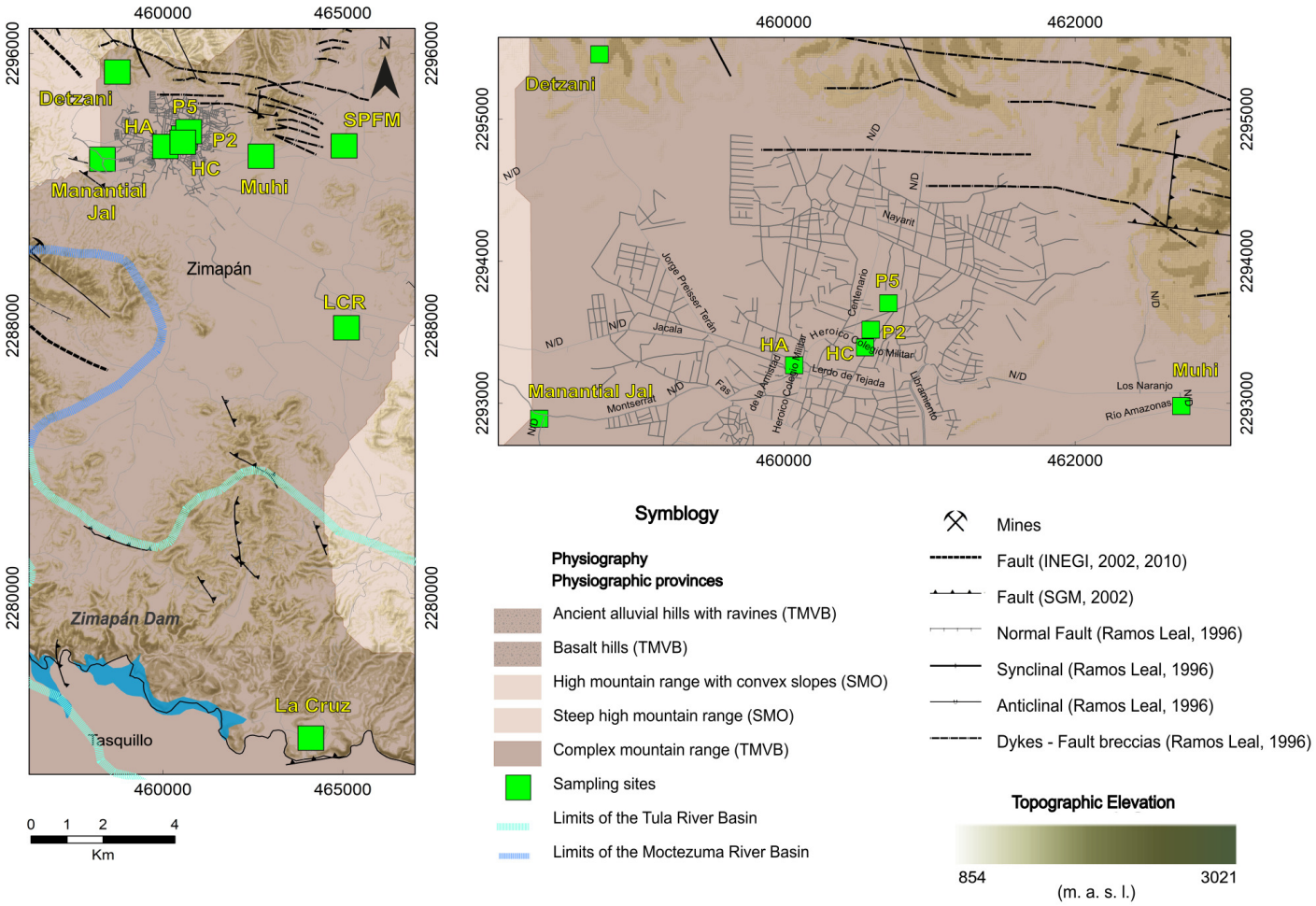


Figure 2. Topographic elevation map as Global Multi-Resolution Topography "GMRT" (Ryan *et al.*, 2009) and sampling sites. Physiography map (INEGI, 2001) with structural parameters from various sources. TMVB = Trans-Mexican Volcanic Belt, SMO = Sierra Madre Oriental. (Derived and modified from INEGI, 2002, 2010; Servicio Geológico Mexicano, 2002; Ramos Leal, 1996).

of the Oligocene. It consists of a fanglomerate with clasts of shale, limestone, and sandstone (Mora, 1998; Martínez Flores & Ortega Gamboa, 2009), with a base covered by fossiliferous limestone. Additionally, there are volcanic rock lenses, such as tuffs near the upper section (Simons & Mapes, 1956). The preceding sequence, up to the Oligocene, is covered by the Las Espinas Formation, distinguished by lavas, tuff deposits, and minor agglomerations, predominantly of andesitic and basaltic composition (Simons & Mapes, 1956).

Nonetheless, Paleocene intrusive bodies are post- tectonic, as they intrude Laramide structures. Their ages range from 50 to 40 million years (Carrillo-Martínez & Suter, 1982; Fitz-Díaz *et al.*, 2012), with varying compositions, ranging from granodiorite to diorite to monzonite to monzogabbro.

Quaternary

During the Holocene, a layer of basic composition lava flows, identified as the Atotonilco Formation (Carrillo-Martínez & Suter, 1982; Mora, 1998; Martínez Flores & Ortega Gamboa, 2009), is situated beneath a polymict conglomerate with fragments of diverse composition known as the Pleistocene Daxi Formation (Simons & Mapes, 1956), which includes andesite rocks, limestone, shales and ashes of diverse composition. Alluvium is ultimately located in the floodplains of rivers and streams (Mora, 1998; Martínez Flores & Ortega Gamboa, 2009), composed mainly of terrigenous deposits, gravel, and predominantly coarse material (Simons & Mapes, 1956).

3.2. Mineralization events

The intrusion of Paleocene granitic-monzonitic rocks into carbonate formations (Mora, 1998), resulted in contact metamorphism and metasomatism (hydrothermal or pneumatolitic) (Simons & Mapes, 1956). Generally, skarn is formed in lime-

stones but it can form in almost any type of rock during regional or contact metamorphism and from a variety of metasomatic processes involving fluids of magmatic, metamorphic, meteoric, or marine origin. They are zoned, and the general pattern is proximal garnet, distal pyroxene, and minerals such as wollastonite, vesuvianite, or massive sulfides and/or oxides near the marble front (Meinert, Dipple & Nicolescu, 2005). Evidence of skarn and varying degrees of contact metamorphism has been identified in the La Encarnación-Villa Juárez location and the Cerro Colorado mining district (Mora, 1998).

3.3. Structural geology

The presence of faults and fractures (Figure 1) is characteristic of this region (Ramos Leal, 1996).

In the Paleocene, the deformation phase corresponding to the Laramide structures began (Carrillo-Martínez and Suter, 1982), with compressive stresses that gave rise to structures of the ductile and ductile-brittle domains, represented by folds and thrust faults (Servicio Geológico Mexicano, 2002). The Laramide deformation style developed along the eastern limestone margin of El Doctor, with a regional N-NW trend (Carrillo-Martínez & Suter, 1982; Fitz-Díaz *et al.*, 2012).

In the Oligocene, monzonite intrusives were emplaced, affecting the previous rocks with contact metamorphism (Servicio Geológico Mexicano, 2002).

In the Miocene, after the end of compressive forces, the relaxation or extensional phase begins, manifested by brittle deformation and the development of post-Laramide structures, such as extensional deformations, compressive structures, and basin-and-range normal faults (Carrillo-Martínez & Suter, 1982; Fitz-Díaz *et al.*, 2012) with NW-SE orientations and dips towards the SW, some with a lateral component that affect the entire sequence (Servicio Geológico Mexicano, 2002).

4. Materials and Methods

4.1. Hydrogeochemistry

In 2022, two sampling campaigns were conducted throughout the rainy and dry seasons, aimed at assessing water quality in wells situated in Zimapán. The sampling procedure followed the guidelines indicated by NOM-014-SSA1-1993 (Secretaría de Salud, 1994), as well as the standard methods of APHA-AWWA (2005), and Mexican norms (NOM-127-SSA1 [Secretaría de Salud, 2022] and NOM-230-SSA1 [Secretaría de Salud, 2005]). Ten sampling sites were selected for this study (Table 1), where field parameters including temperature, pH, oxidation-reduction potential and electrical conductivity were measured at each location using a HANNA-HI98194 multiparameter device (Hanna Instruments Inc., 2020). Calibration was performed prior to the measurements at each sampling point, utilizing Quick Cal calibration solution (HI9828-0) for pH and electrical conductivity, while for the oxidation-reduction potential, ORP was calibrated with Zobell solution.

The chemical analysis of major ions was conducted in accordance with the APHA-AWWA methods (APHA-AWWA, 2005) at the Analytical Chemistry Laboratory of the Institute of Geophysics, UNAM, Mexico, using standard procedures. Bicarbonate was quantified using volumetric titration with HCl, Cl^- was analyzed by potentiometry with selective electrodes (4500-Cl^-), and SO_4^{2-} was determined by turbidimetry (method 4500-SO_4^{2-}). Ca^{2+} and Mg^{2+} were analyzed by volumetry (EDTA titration); while Na^+ and K^+ were determined by atomic emission spectrophotometry (3500-Na^+ and K^+), SiO_2 was determined using flame atomic absorption spectrophotometry and UV-visible spectroscopy (molybdosilicic acid method). The analytical quality was assessed using ionic balance (below 10%) and the utilization of certified reference solutions (traceable to NIST).

4.2. Geophysics

The study region was selected for 3D geophysical modeling based on the hydrogeochemical results from the sample stations, using potential field data. Magnetic Anomaly and Bouguer Anomaly data sets were collected, adapted, and processed using Oasis Montaj (2024.1) (Seequent, 2024). Both datasets encompass a region of 2321 km^2, including the municipality of Zimapán and its vicinity.

We utilized data obtained from the Magnetic Anomaly Map of North America (2002) sourced from the USGS geophysical database (North American Magnetic Anomaly Group *et al.*, 2002), which exhibits an average separation of 914 m. This subsequently produces areas of 835,306 m^2. The data can be accessed and downloaded from GeoMapApp (**www.geomapapp.org**) in various formats for later manipulation. The national compilation included in the North American database for the research area was obtained by the Mineral Resources Council of Mexico (CRM) with a cell size of one-fifth of the flight line spacing, utilizing a minimal curvature algorithm (North American Magnetic Anomaly Group *et al.*, 2002). We utilized the ICGEM platform, employing the gravimetric satellite dataset of the EIGEN-6C4 model, which offers the best global resolution and coverage, effectively delineating deep anomalies with commendable precision (Camacho & Alvarez, 2021). This dataset has an average separation of 107 m producing areas of 11,450 m^2.

Table 1. Catalog of sample locations in the Zimapán region, Hidalgo.

Code	Name	Type of structure	UTM X (mE)	UTM Y (mN)	Elevation (m.s.n.m.)	Well depth (meters)	Estimate d depth S.W.L. (meters)
Detzani	Detzani	Well	485409	2134773	1829	≈90	≈ 70
P2	Pozo 2	Noria	460596.1	2293517.9	1793	30	N/A
P5	Pozo 5	Well	460718	2293704.6	1802	125	≈ 67
HC	Heroico Colegio	Well	460557.4	2293394.8	1790	18	≈18
HA	Hotel Ányelo	Noria	460070.6	2293268	1743	11	11
El Muhi	El Muhi	Well	462728.9	2292981.1	1790	200	≈100
SPFM	San Pedro Fosforita México	Well	465049.72	2293300.19	1840	200	≈25
LCR	Lázaro Cárdenas Remedios	Well	465084.92	2287922.29	1862	≈90	≈ 80
La Cruz	La Cruz	Well	465275	2276061	1625	300	≈90
Mananti al Jal	Mananti al Jal	Spring	458320.1	2292892	1747	N/A	N/A

Data with symbol "≈" were estimated from indirect measurements with PQWT -TC500 water detector.

For the 2D models of the magnetic anomaly, the residual effect was derived from its power spectrum, followed by the execution of Pole Reduction (PR). The generated map serves as the foundation for the derivative applied in "x" aimed at identifying anomalies that may align with the orientation of the predominant faults in the study area, and subsequently tracing lineaments (possible geological limits, faults or fractures), as well as delimiting edges and areas of high gradient to facilitate integration and to be able to relate to these geological structures. Next, the Analytical Signal filter was applied to the base map to correlate the magnetic response of the prevalent materials in the study area and to identify Aeromagnetic Domains (AMD's). The residual effect of the Bouguer anomaly was extracted from its power spectrum, and the vertical derivative was applied to emphasize surface anomalies potentially associated with the terrain and, in certain instances, with previously identified geologic structures.

Two polygons were generated for the 3D modeling, concentrating on the sampling points (Ply1 and Ply2). The initial polygon (Ply1) has an area of 225 km^2, and the 3D model obtained from this polygon and the terrain's topography possesses a volume of 1236.15 km^3, a thickness of 5.494 km, and a resolution of 500 m. Utilizing 300 real data points for the inverse model of the Magnetic Anomaly and 20,097 real data points for the inverse model of the Bouguer Anomaly.

The second polygon (Ply2) encompasses an area of 48.61 km², yielding a 3D model with a thickness of 3.527 km and a resolution of 250 m, utilizing 55 real data points for the inverse model of the Magnetic Anomaly.

5. Results

5.1. Hydrogeochemistry

The findings indicate that the wells with elevated arsenic concentrations specifically HA, SPFM, P2, P5 and Detzani (from 0.029 to 1.212 mg/L of arsenic in drinking water), located in the central zone of the municipality, surpassed the permissible limit stipulated by NOM-127-SSA1-2021 and the WHO guidelines for drinking water (Table 2).

All wells exhibit a pH range of 7.15 to 7.98, indicating that the groundwater traverses an alkaline environment.

The sampling points situated in the Moctezuma River basin (fractured Cretaceous limestones, [Armienta *et al.*, 2001]), including P2, P5, Detzani, SPFM and Muhi, display intermediate electrical conductivity values ranging from 424 to 692 µS/cm and exhibit a marginal rise in temperature, Muhi representing the upper limit of this range at 31.84 °C. The noria (shallow well) HA records a relatively low temperature with a high E.C. (740 µS/cm) similar to the rest of the deeper wells. While in Manantial Jal, despite recording the highest arsenic concentration and the maximum electrical conductivity value (2850 µS/cm), the measured temperature was 22.35 °C, which is comparable to the average air temperature in that time of the year (22 °C).

On the other hand, the wells situated in the Tula River basin (volcanic setting) and a small portion of the Moctezuma River basin, including La Cruz and LCR, exhibit slightly elevated temperatures, ranging from 22.74 to 26.9 °C, without exceeding

Table 2. Concentrations of major and trace elements and physicochemical parameters of groundwater samples collected in the study area.

Well	pH	T (°C)	C.E.	Na^+	K^+	Ca^{2+}	Mg^{2+}	Cl^-	SO_4^{2-}	HCO_3^-	SiO_2	F^-	As
			µS/cm	mg/ L	mg/ L	mg/ L	mg/ L	mg/ L	mg/ L	mg/ L	mg/ L	mg/ L	mg/ L
NOM-127-SSA1-2021 (mg/L)				N/A	N/A	N/A	N/A	N/A	400	N/A	N/A	1.5	0.025
P2	7.47	25.53	433	14.7	1.77	58.33	12.1	11.3	31.04	222.94	25.04	0.19	**0.107**
P5	7.5	29.2	531	8.56	1.07	79.01	16.9	7.49	62.96	239.22	15.62	0.715	**0.516**
Detza ni	7.24	26.5	692	9.75	0.85	110.7	19.39	8	156.9	264.33	12.28	0.435	**0.81**
HA	7.25	21.59	740	17.25	2.3	123.1	7.52	29.5	82.52	270.61	12.92	0.202	**0.029**
La Cruz	7.98	26.9	878	86.1	7.47	57.26	24.88	73.2	104.4	260.15	69.33	0.463	0.006
LCR	7.41	22.74	561	19.9	2.76	75.39	15.34	12.5	43.12	294.24	30.51	0.333	0.004
SPF M	7.35	24.34	691	24.21	2.94	80.16	28.93	12.5	45.9	382.75	43.12	0.773	**0.061**
Man. Jal	7.6	22.35	2850	76.55	25.38	572.6	52.1	100	**1622**	364.8	20.11	**1.34**	**1.866**
El Muhi	7.16	31.84	567	42.1	3.8	56.69	20.2	5.97	67.67	282.24	16.22	**2.3**	**1.212**

*Values highlighted in bold are those that exceed the limits established by the NOM-127-SSA1-2021 in the study area.

those recorded in the central wells. La Cruz shows the highest E.C. within this group (878 µS/cm).

The Piper diagram (Figure 3a) indicates that the majority of samples exhibit a chemical composition that varies from calcium-bicarbonate to calcium-sulfate, except for La Cruz well, situated to the southeast part of the study area, which plots within a water mixing field. This well, as well as LCR, exhibit As concentrations below the limits established by NOM-127-SSA1-2021.

The D'Amore diagram (Figure 3b) show distinct groupings and trends among the sampled wells based on major ion composition (D'Amore *et al.*, 1983). Manantial Jal displays a distinctive ion pattern compared to other sample locations, while La Cruz, El Muhi, and Detzani show differentiated trends to a lesser extent.

In the diagram of mineral dissolution and alteration processes (Figure 4) the HCO_3/SiO_2 versus Mg/(Mg+Ca) ratio differentiates between carbonate and silicate alteration domains, with HCO_3/SiO_2 values exceeding 10 indicative of carbonate dissolution, whereas values below 5 signify silicate alteration (Hounslow, 2018). These processes mainly cause the degradation of feldspars to kaolinite, sericite, epidote and quartz through hydrothermal alteration processes of propylitic, argillic and phyllic type (Simons & Mapes, 1956).

During carbonate interaction, water exhibits an increase in alkaline-earth elements (though a comparable response may occur with felsic rocks), and diminished concentrations of alkaline elements; conversely, silicate alteration results in an opposite scenario (Clark, 2015).

5.2. Geophysics

5.2.1.Gravimetric data

The Bouguer anomaly reveals variations in subsoil density by correcting for the topographic effect, which allows these anomalies to be related to or differentiated from topography and thus identify possible underground structures. Therefore, to differentiate whether a gravimetric anomaly is associated with the topography or indicates an underground structure, the Global Multi-Resolution Topography (Ryan *et al.*, 2009) was used (Figure 5a).

Simple Bouguer Anomaly data obtained from the ICGEM platform utilized the gravimetric satellite data set of the EIGEN-6C4 model. A spectrum analysis was performed to separate the regional and residual effects, with the latter utilized for the following application of the vertical derivative (Figure 5b) and for the data inversion that ultimately produced the 3D density model.

5.2.2. Aeromagnetic Data

The magnetic data enabled the identification of lineaments (Figure 6) in the study area that correspond with faults documented in prior research (Ramos Leal, 1996; Servicio Geológico Mexicano, 2022).

The analytical signal map (Figure 7) illustrates surface structures linked to three Aeromagnetic Domains (AMD's).

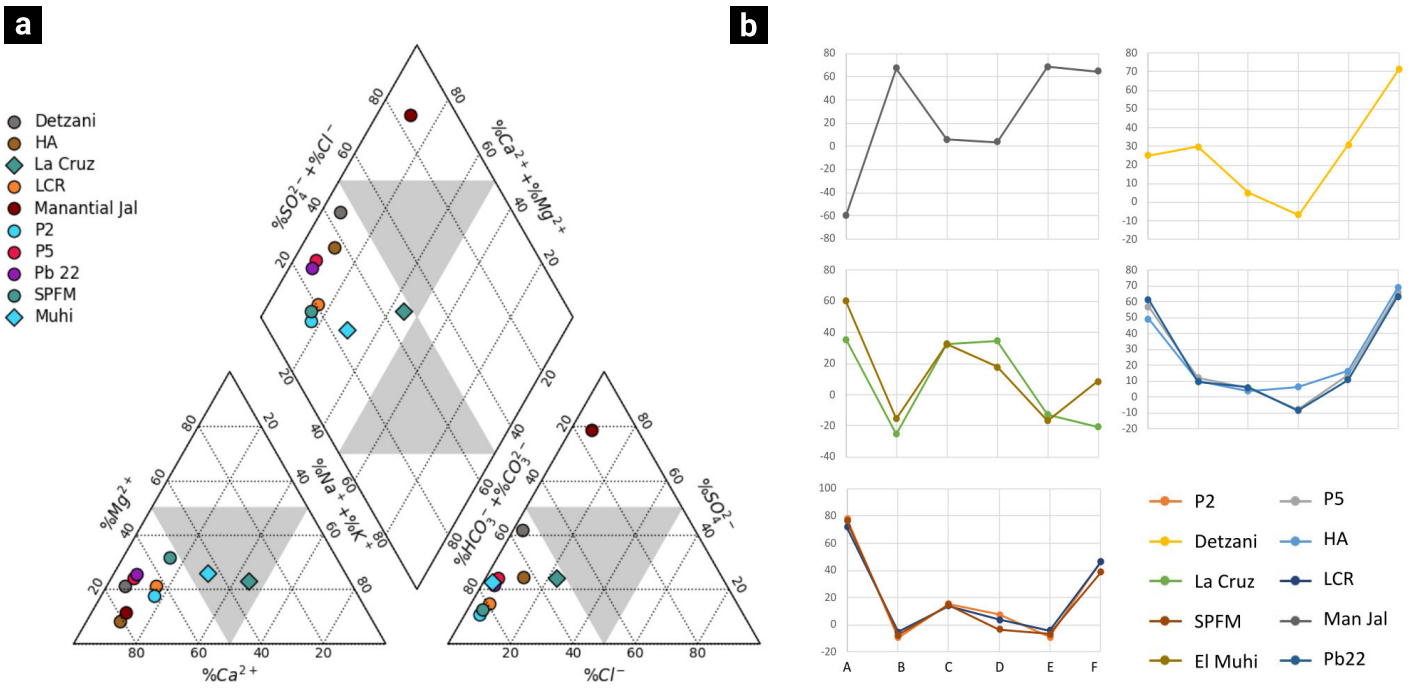


Figure 3. a) Piper diagram of the well samples collected in the groundwater of Zimapán, Hidalgo. b) Diagram of D'Amore *et al.*, 1983, applied to the groundwater of Zimapán, Hidalgo: $A = 100\left[\frac{HCO_3 - SO_4}{\sum(-)}\right]; B = 100\left[\left(\frac{SO_4}{\sum(-)}\right) - \left(\frac{Na}{\sum(+)}\right)\right]; C = 100\left[\frac{Na}{\sum(+)} - \frac{Cl}{\sum(-)}\right];$ $D = 100\left[\frac{Na - Mg}{\sum(+)}\right]; E = 100\left[\frac{Ca+Mg}{\sum(+)} - \frac{HCO_3}{\sum(-)}\right]; F = 100\left[\frac{Ca - Na - K}{\sum(+)}\right]$ *where* $\sum(-) = anions$ *and* $\sum(+) = cations.$

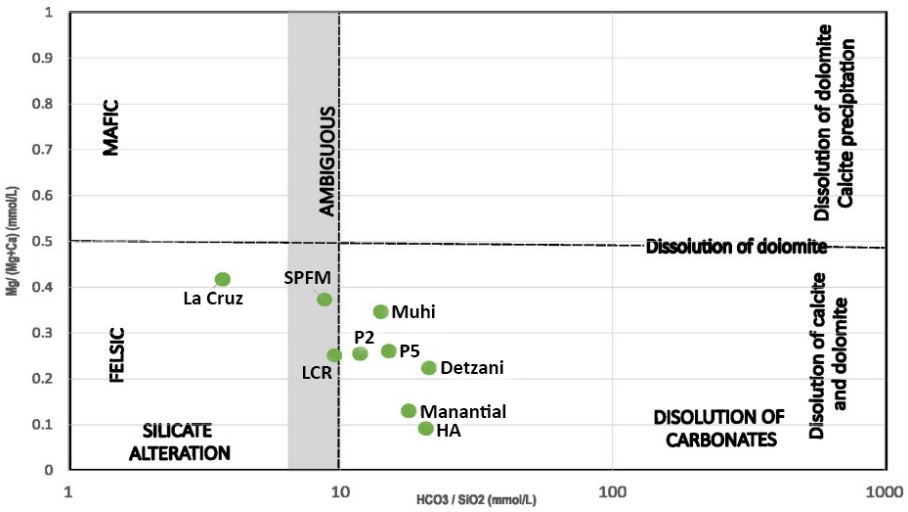


Figure 4. Diagram illustrating mineral alteration and dissolution processes (Hounslow, 2018) in the groundwater of Zimapán, Hidalgo.

The clustered wells in the central zone of the municipality are situated along the boundary between AMD I and AMD II, whilst the SPFM, LCR, and La Cruz wells are positioned within AMD II.

AMD I (0 to 0.002 nT/m): Denotes the lowest analytical signal values. It covers the northern region of the map, defined by the El Doctor formation and the Soyatal formation, featuring a series of limestones, flint bands, and calcareous breccias within the Sierra Madre Oriental (López, 2008).

AMD II (0.007 to 0.017 nT/m): encompasses a NE-SW-oriented region within the study area, indicating the highest values of the map. This domain consists mostly of volcanic rocks from the Las Espinas formation and rhyolitic deposits, along with contact zones between sedimentary and igneous rocks. Towards

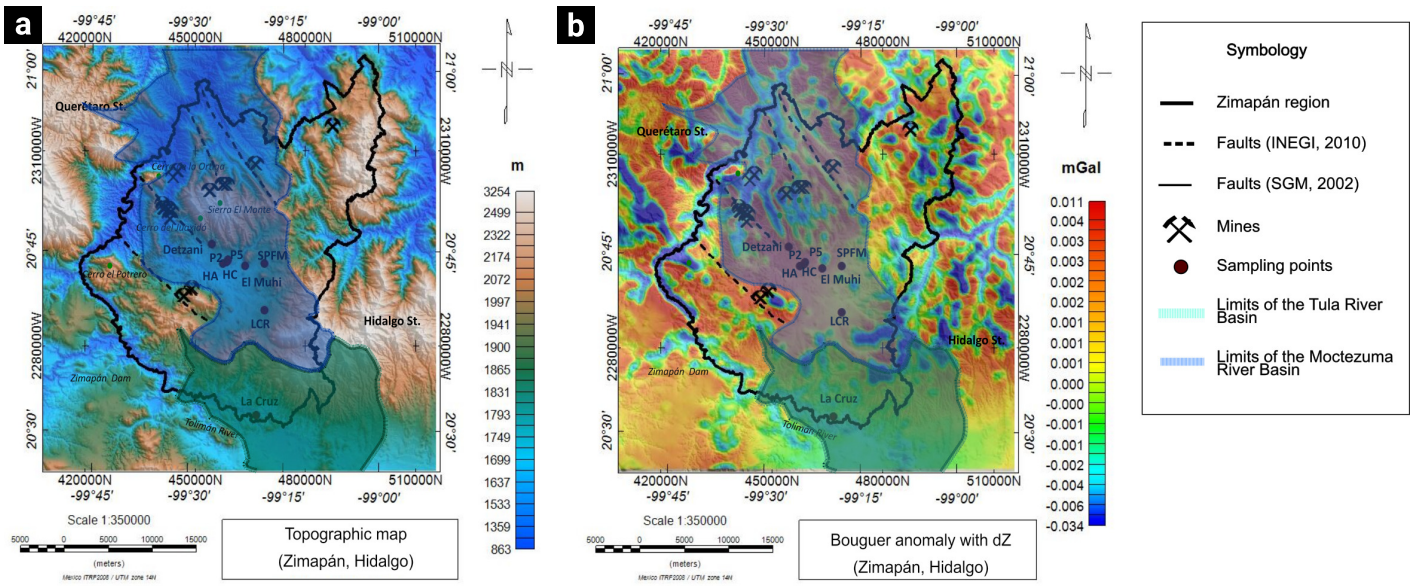


Figure 5. a) Topography (GMRT) in Zimapán, Hidalgo (Ryan *et al.*, 2009). Depiction of relief, faults, mines and groundwater extraction wells. b) Map of the Simple Bouguer Anomaly with vertical derivative in Zimapán, Hidalgo.

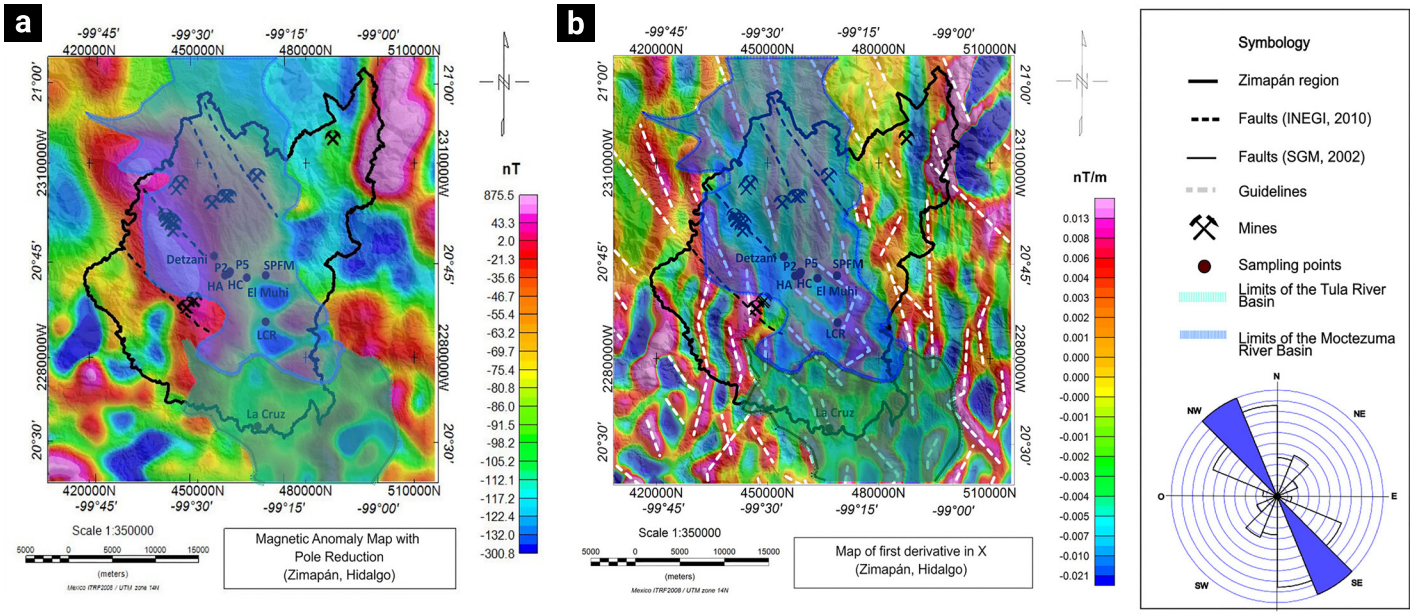


Figure 6. a) Magnetic Anomaly Map with Pole Reduction. b) Map of the first derivative in "x" with Pole Reduction of the residual effect on the Magnetic Anomaly. Rosette illustrates the preferred orientation of the NW-SE lineaments.

the center of this domain, the El Morro formation is present, which holds significant economic value due to the presence of valuable minerals. It is a polymictic conglomerate composed of limestone pieces, andesites, and a calcareous matrix containing quartz, feldspar, and mica (López, 2008).

AMD III (0.002 to 0.007 nT/m): It is formed by a contrast of very high and low values of the analytical signal. Intrusive igneous rocks of granodioritic composition are present, containing minerals such as quartz, sodium plagioclase, potassium feldspar, hornblende, biotite, sphene, apatite, and zircon (López, 2008). Nonetheless, there exist interactions between these crystalline entities and sedimentary formations; however, in contrast to AMD II, the surrounding environment is primarily volcanic, as it shares the same chemistry as plutonism.

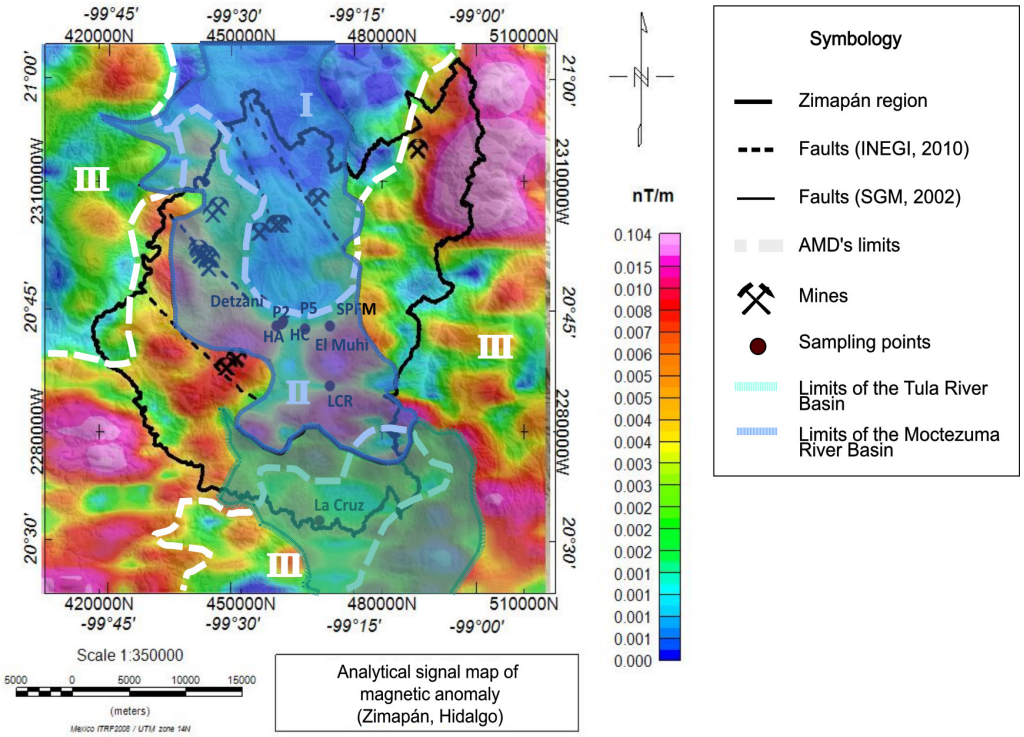


Figure 7. Analytical Signal Map of the Residual Effect of the Magnetic Anomaly. III AMD's (Aeromagnetic Domains) were identified.

5.2.3. 3D Inverse Model

For structural geological characterization, inversion was conducted on both potential datasets utilizing polygons (Ply1 and Ply2) that defined two areas of interest. The 3D models of the Magnetic Anomaly delimit distributions of different materials with their corresponding magnetic susceptibility value [SI] in both polygons (Figure 8).

Conversely, the 3D model constructed from the Bouguer Anomaly and utilizing Polygon 1 demonstrates a density distribution with a standard reduction density of 2.67 g/cm^3, which is conventionally employed for calculating the Bouguer Anomaly and serves as a reference in this instance, as established at the onset of the data inversion (Ayala & Rey, 2009). This indicates that the density variations within the model are assessed relative to this standard, regarded as the baseline of its measurement scale.

The 3D model derived from Polygon 1 confirms the presence of highly dense bodies associated with granitic-monzonitic intrusions during the Laramide Orogeny (Figure 8. Isosurface 1), which, based on its value range, corresponds to acidic igneous rocks, metamorphic rocks, granite, and quartz. Mineralization is observable above and around these bodies (Figure 8. Isosurface 2), which, based on its value range, may be related to certain sulfides, igneous and sedimentary rocks (Table 3).

Upon examining solely, the peak values of both 3D models (Figure 8), it is evident that the mineralization correlates with the presence of the highly dense bodies 1 and 2, and that seemingly interlinks both bodies, exhibiting a distinct directional distribution (NW-SE), potentially influenced by geological faults identified in the 2D maps (Figure 6).

To enhance understanding of the distribution of magnetic susceptibility values and densities, four sections were created based on two profiles that intersect several boreholes in both carbonate and volcanic environments.

Distribution of mineralization correlated with material with magnetic properties (Isosurface). Also included is the topographic map superimposed with both 3D models, illustrating the geographic position of the wells under investigation.

Sections 1a and 1b (Figure 9) intersect with the Muhi well and extend towards the SPFM well, where the lowest susceptibility values (Figure 9. 1b) and Figure 10. 2b), around -0.00031 SI) align with those of calcite [$CaCO_3$] (Table 3., M.S. Calcite = around -0.00001 SI). Conversely, the highest magnetic susceptibility values may be indicative of sulfide mineralization located within the transition zone of densities, suggesting the potential emplacement of the carbonate sequence by a granitic intrusion. This cavity is located near a surface body of low density, such as the Muhi, which may be associated with groundwater. A normal type of fault was detected near the Muhi well, indicated by alterations in terrain and a significant discrepancy in density. The HA well is located within a density transition zone; nonetheless, substantial mineralization is absent.

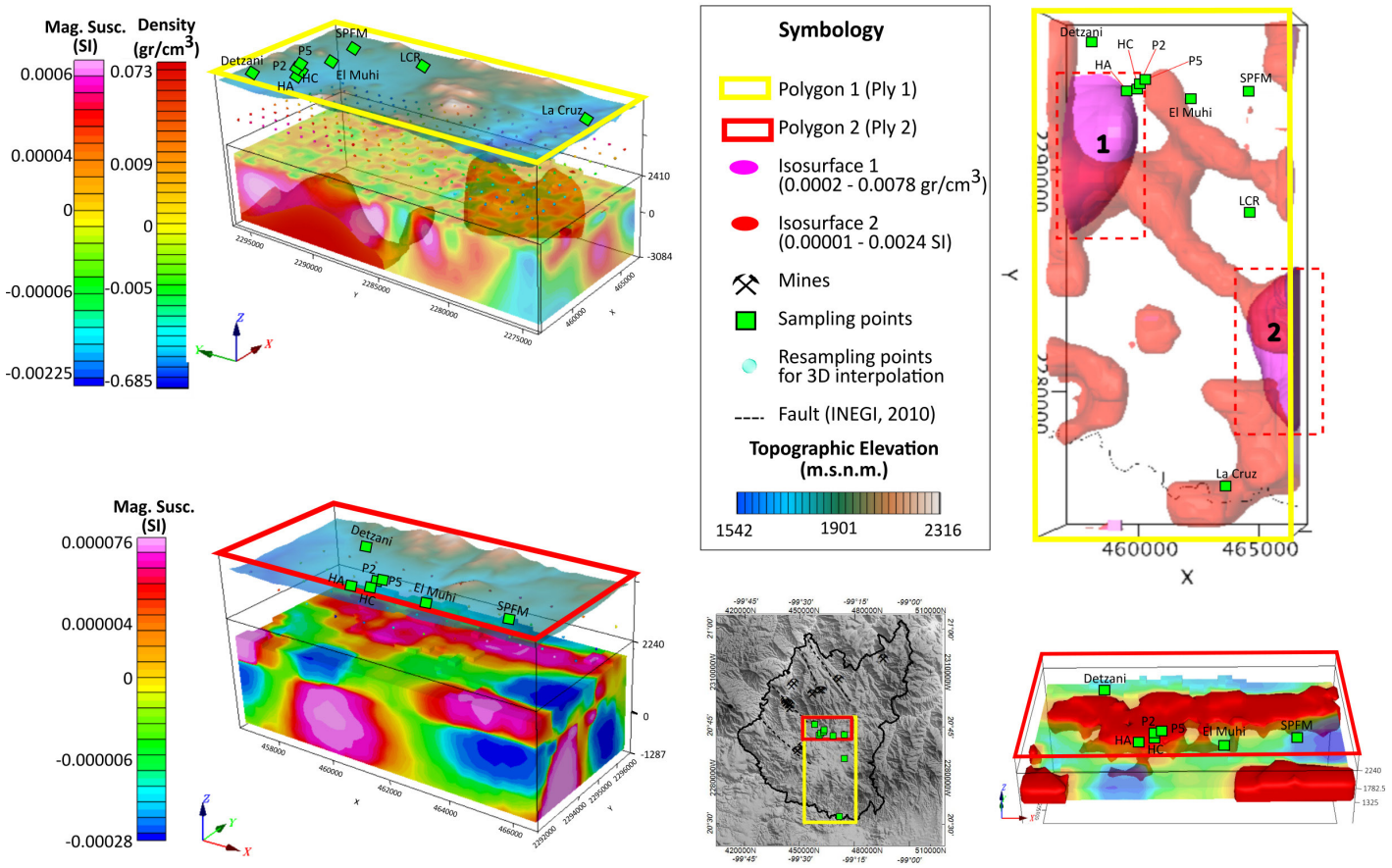


Figure 8. Three-dimensional models created from Polygon 1 and Polygon 2. To the right is the locational map of highly dense bodies (isosurface 1) linked to granitic intrusive bodies 1 and 2. Together it shows mineralization (isosurface 2) linked to orogenic faults (Servicio Geológico Mexicano, 2002).

Table 3. Density and magnetic susceptibility ranges for various rocks and minerals

	Density (g/cm³)	Magnetic Susceptibility x10³ (SI)
Minerals		
Sphalerite	3.5 – 4	0.7
Chalcopyrite	4.1 – 4.3	0.4
Pyrrhotite	4.5 – 4.8	1500
Pyrite	4.9 – 5.2	(0.005 – 5) 1.5
Arsenopyrite	5.9 – 6.2	2.5
Kaolinite	2.2 – 2.63	
Gypsum	2.2 – 2.6	-0.01
Calcite	2.6 – 2.7	-0.001 - -0.01
Quartz	2.5 – 2.7	-0.01
Rocks		
Acid igneous	2.3 – 3.11	0 – 80
Granite	2.5 – 2.81	2.5
Shale	1.77 – 3.2	0.6
Limestone	1.93 – 2.9	0.3
Dolomite	2.28 – 2.9	0.1
Sedimentary rocks	2.5	0.9
Metamorphic rocks	2.4 – 3.1	4.2

* Data sourced from Telford *et al.*, 1990.

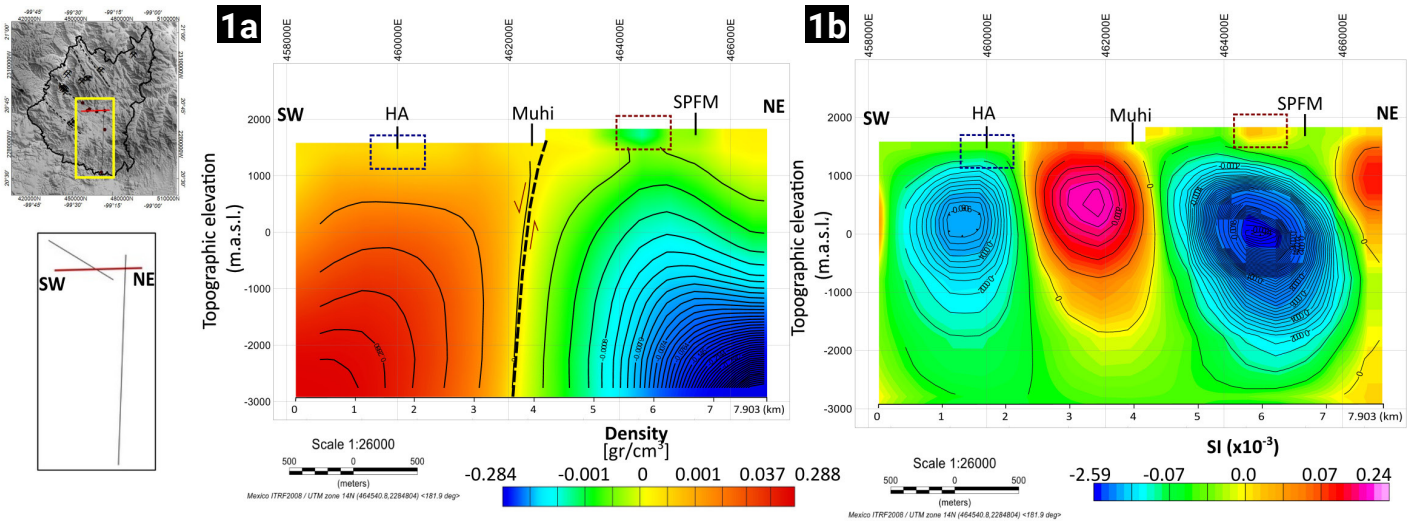


Figure 9. Section 1a: Derived from the 3D inverse model of the Bouguer Anomaly utilizing profile 2 (Data obtained and modified from the ICGEM EIGEN-6C4 database with a resolution of 0.001°). Section 1b: Derived from the 3D inverse model of the Magnetic Anomaly based on profile 2 (Data obtained and modified from the Magnetic Anomaly Map of North America, USGS, 2002).

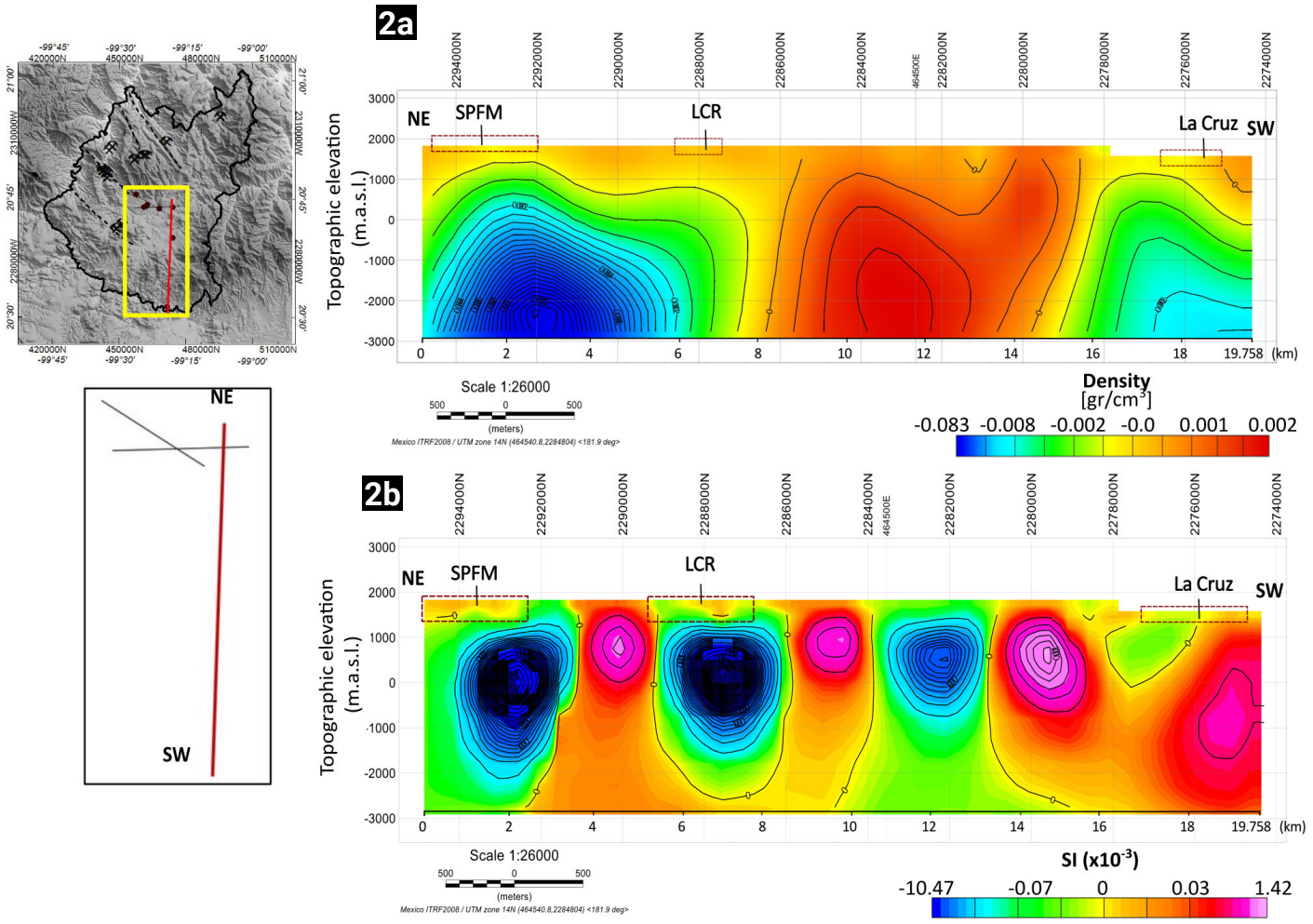


Figure 10. Section 2a: Derived from the 3D inverse model of the Bouguer Anomaly, utilizing profile 3 (Data sourced and altered from the ICGEM EIGEN-6C4 database with a resolution of 0.001°). Section 2b: Derived from the 3D inverse model of the Magnetic Anomaly based on profile 3 (Data sourced and altered from the Magnetic Anomaly Map of North America, USGS, 2002).

Section 2a and 2b (Figure 10) extend from northwest to southwest, encompassing the SPFM, LCR and La Cruz wells, which are situated within mineralized zones of a superficial nature. However, these zones are in areas of intermediate density that do not align with contact zones between potential intrusive granitic bodies and the carbonate sequence, suggesting an association with the volcano-sedimentary deposits of the Las Espinas Formation. Regionally, there is a marked distribution of low density oriented towards the northeast, suggesting a sedimentary and carbonate environment, but to the southwest, the density increases, indicating the dominance of a volcanic environment.

6. Discussion

6.1. Hydrogeochemistry

The hydrogeochemical results show high arsenic concentrations in several of the water extraction wells (Table 2); according to previous results, these high values could be related to geological faults, that significantly contribute to the transport of arsenic to deep wells (Armienta *et al.*, 2001), as evidenced by the distribution of lineaments and faults detected in this study, which used geophysical methods and the local geology (Figure 1, Figure 2 and Figure 6), and are located in the same areas as the wells with the highest As values.

The physicochemical parameters taken at the sampling points, situated in fractured Cretaceus limestones, indicate that this phenomenon has been associated with exothermic oxidation reactions of sulfides, such as arsenopyrite (Armienta *et al.*, 2001). Besides, the physicochemical parameters in Manantial Jal indicate that the increase in total dissolved solids is not driven by a thermal source, but is instead primarily associated with the proximity of mine waste, which contributes dissolved constituents to the aquifer system (Sracek *et al.*, 2010).

The Piper and D'Amore diagrams highlight differences in the ionic composition of the water samples, which are linked to distinct geological formations and hydrogeochemical processes (e.g. dissolution or mineral alteration) (D'Amore *et al.*, 1983). Most wells exhibit a dominance of HCO_3^- over SO_4^{2-} (Facie A), in addition, it is observed that in several wells the Na^+ content is representative of an environment where clayey material dominates. Detzani, P5, HA and LCR wells, and Manantial Jal show a relatively higher SO_4^{2-} content (Facie B); in the case of Na^+ and Cl^- ratio, sodium is dominant and they have a slight similarity in concentration, which suggests dissolution of halite or alteration of Na plagioclase (Facie C); with respect to the Mg^{2+} and Ca^{2+} ratio, most of the wells show a possible participation of calcite, dolomite and silicate alteration (Facie D); with respect to the source of Ca^{2+}, Mg^{2+} and HCO_3^-, half of the wells show carbonate dissolution processes and the other half show sulfate interaction (Facie E), it should be noted that sulfates could also come from the oxidation of sulfides; and finally, in most of the wells there is a K contribution due to the alteration of Ca silicates and only one well shows alteration of K-Na silicates (Facie F).

This is supported by the HCO_3/SiO_2 vs $Mg/(Mg+Ca)$ diagrams (Hounslow, 2018), which align with findings from other studies conducted in proximity to the research area (González-Partida *et al.*, 2003), specifically on reef limestones exhibiting hydrothermal alteration (Corona-Esquivel & Sanchez-Loyo, 2022). It is significant that, despite the widespread presence of carbonate rocks, which typically promote HCO_3^- enrichment through dissolution processes, the observed variability in major ion chemistry suggests the influence of additional lithological controls or geochemical processes. In particular, the anomalous behavior of sodium indicates a contribution from the alteration of sodium-bearing silicate minerals, such as sodium plagioclase, which are abundant in felsic volcanic and intrusive rocks. This interpretation is supported by previous mineralogical and geochemical analyses conducted on the minerals of the mine tailings in the study area (Moreno Tovar *et al.*, 2012), which report homogeneous concentrations of Na_2O and P_2O_5 with average values of 0.61% and 0.12% respectively. These elemental signatures are characteristic of felsic intrusive lithologies and indicate a persistent source of sodium (Moreno Tovar *et al.*, 2012).

The Piper diagram illustrates a chemical composition that varies from calcium bicarbonate to calcium sulfate (mainly Manantial Jal). The La Cruz well plots separately from the main group, reflecting a distinct hydrogeochemical characteristics, associated with mixing processes rather than a single dominant water-rock interaction pathway (Figure 3). This well, is situated in a region characterized by minimal effect from the mineralization, identified by the geophysical method (Figure 8, Isosurface 2), and on a volcanic-sedimentary substrate. These conditions suggest that the observed chemical composition at La Cruz is controlled by the convergence of waters with different geochemical characteristics and by limited interaction with mineralized carbonate or sulfide-bearing formations. Consequently, the hydrogeochemistry of the La Cruz well reflects a geologically constrained system with reduced mineralization influence compared to the central carbonate-dominated zones.

The hydrogeochemical results indicate that the shallow groundwater that reaches the Manantial Jal explains the high concentration of arsenic and sulfates due to its proximity to a mining tailings, thus classifying it as a point source of contamination. (Sracek *et al.*, 2010).

6.2. Geophysics

The utilization of airborne magnetometry reveals notable anomalies in the studied area. The lineaments identified with the application of the first derivative in "x" suggest the potential presence of faults and fractures, as evidenced by the peaks at the sources that denote contours characterized by abrupt gradients and inflections (Milligan & Gunn, 1997) (Figure 6b). These lineaments align with the orientation of the Bouguer Anomaly and the vertical derivative (Figure 5), and it is noted that the high peaks on this map do not invariably correspond to topographic elevations. Consequently, it is inferred that the structures observed at the surface may extend to depth, as indicated by these anomalies. The use of the Analytical Signal facilitates the identification of Aeromagnetic Domains (DAMs), which are indicative of the local geology (Figure 7) (López-Loera & Tristán-González, 2013). The results are geologically analogous, rendering these geophysical discoveries essential for comprehending the distribution of minerals and rocks in the subsurface, as well as for pinpointing regions of geoeconomic significance and potential environmental hazards.

The 3D models enable the examination of density distribution and magnetic susceptibility from the topographic level and 5,494 m thickness. The occurrence of contact zones between granitic intrusions and the carbonate series is substantiated, resulting in contact metasomatism accompanied by hydrothermalism. These connections may correlate in the 3D model of the Bouguer anomaly of Polygon 1 with the transition zones that surround mineralization by iron sulfides, indicated by elevated values of magnetic susceptibility. Conversely, the 3D model derived from Polygon 2 exclusively yielded the inversion of the Magnetic Anomaly data for the central wells, as the objective was to distinctly visualize the mineralization distribution and its potential impact on the water quality of the wells in this region, taking into account a thickness measured from the topographic level to the maximum depth of the wells (La Cruz = 300 meters). Mineralization is less intense than in Polygon 1, occurring sporadically along the interfaces of igneous and/or volcanic rocks and sedimentary rocks. However, the Detzani Well is situated directly above the mineralization, while HA, P5, P2, and HC are in its proximity. The Muhi and SPFM wells do not intersect the mineralization.

6.3. Arsenic pollution

The central wells are situated in a predominant carbonate environment and near thick granite bodies, together with mineralization characterized by magnetic data (Figure 8, Isosurface 2), as well as in multiple studies where mineral deposits related to metallic sulfides were characterized using magnetic prospecting for exploration (Morgan, 2012; Airo & Loukola-Ruskeeniemi, 2004; Vallée, Moussaoui and Khan, 2024). The mineralization distribution aligns with the NW-SE geophysical lineaments (Figure 6) and with the geological faults identified in prior research (Servicio Geológico Mexicano, 2022). Consequently, it is inferred that these faults extend into depth and interconnect intrusive bodies 1 and 2 (Figure 8). Structures like faults can enhance the secondary porosity and permeability of the aquifer system (Alt-Epping *et al.*, 2022). Consequently, an understanding of the local geology and Paleocene occurrences (skarn and hydrothermalism) suggests that mineralization potentially occupying the faults is predominantly composed of iron sulfide minerals. This is supported by geophysical interpretation (Figure 8), which indicates that upon contact with water, these minerals can leach highly toxic metals and metalloids, such as arsenic.

In groundwater research, it would be ideal to work with higher-resolution potential field data; nonetheless, in this instance, it was adequate to analyze the mineralization distribution responsible for arsenic pollution, considering the wells' maximum depths. Furthermore, it was determined that the contamination disseminates in relation to the direction of groundwater flow, the proximity of the wells to the mineralization, and the existence of geological faults (Figure 11).

Additionally, the piezometric levels indicate a shallow aquifer system (e.g., HA or P2: approximately 20 meters) where contamination is minimal and corresponds to low magnetic susceptibility values. Moreover, in these cases, the influence of geological faults or fractures is not significant, unlike in the case of deeper wells (e.g., Muhi, SPFM: approximately 200 meters).

This latter scenario of a deep aquifer system is exemplified by the Muhi well, which is situated in a contact zone between materials of varying densities, exhibiting pronounced mineralization associated with metallic sulfides. Additionally, it is situated near an inferred fault (Muhi Normal Fault), which aligns with geophysical findings and indicates a tendency towards a mixing zone, as determined by hydrogeochemical analysis.

This finding underscores that arsenic contamination is influenced by mineralization associated with granitic intrusions, primarily composed of arsenopyrite ($AsFeS_2$), scorodite ($FeAsO_4{\cdot}2H_2O$; an oxidation product of arsenopyrite), freibergite [$(Ag, Cu, Fe)_{12}$ $(As,Sb)_4S_{13}$], and proustite (Ag_3AsS_3), which formed through the interaction of these crystalline bodies with carbonates (Armienta *et al.*, 2001; Moreno Tovar *et al.*, 2012). Accordingly, oxidation of arsenopyrite and pyrite was incorporated into the mineral dissolution–equilibrium reactions used in inverse modeling calculations, and arsenopyrite dissolution together with scorodite precipitation and dissolution were considered as key processes contributing to the observed increase in arsenic concentrations (Armienta *et al.*, 2001).

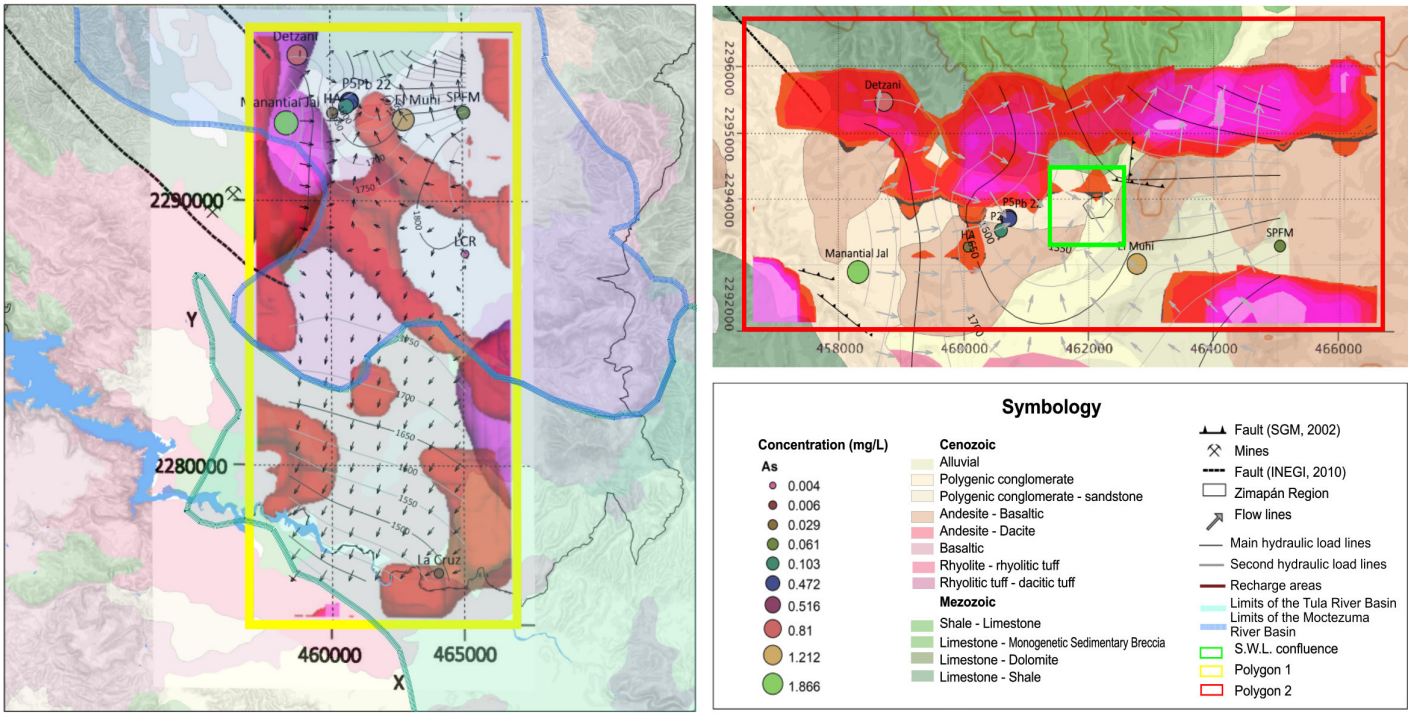


Figure 11. Arsenic concentrations in wells located within the geological map of the region and the mineralization identified throw the geophysical method. The groundwater flow network was estimated from indirect measurements with PQWT- TC500 water detector (Table 1). *S.W.L. Confluence = Static Water Level Confluence).

Consequently, factors such as fault-hosted mineralization, the proximity of water extraction wells to the faults, and the direction of groundwater flow may influence the presence of arsenic in groundwater.

7. Conclusions

The application of geophysical techniques in elucidating the geological context of the central Zimapán municipality proved effective for identifying crystalline bodies associated with granitic intrusions. These intrusions, upon interacting with the carbonate sequence of the Soyatal and Doctor Formations, generated contact zones potentially linked to contact metasomatism and hydrothermal activity. Moreover, the correlation between these bodies was identified as the existence of mineralization linked to iron sulfide deposits, which occupy the geological faults within the research area. According to the geophysical and hydrogeochemical results, the contamination is primarily attributable to a combination of three factors: the direction of groundwater flow, the presence of mineralization, and proximity to fault-type geological structures. Consequently, while other contaminant sources exist in this area, the predominant source is of natural origin. The amalgamation of geophysical and hydrogeochemical techniques in the examination of the Zimapán aquifer has yielded a comprehensive understanding of its underlying dynamics and water quality. The detection of fault-related lineaments, densely concentrated bodies, and mineralization linked to iron sulfides, together with their association to arsenic distribution, underscores the efficacy of integrating both approaches.

8. Acknowledgements

We express our gratitude to O. Cruz, A. Aguayo and O. Neri from the Laboratorio de Química Analítica of the Institute of Geophysics, to PAPIIT for providing the economic resources to finance this project, PAPIIT IN105023. The Secretaría de Ciencia, Humanidades, Tecnología e Innovación (Secihti), where the first author is currently a Secihti scholarship holder at the graduate level.

9. References

Alabi, A. A., Popoola, O. I., Olurin, O. T., Ogungbe, A. S., Ogunkoya, O. A., & Okediji, S. O. (2020). Assessment of groundwater potential and quality using geophysical and physicochemical methods in the basement terrain of Southwestern, Nigeria. *Environmental Earth Sciences*, 79, 1-13. doi: https://doi.org/10.1007/s12665-020-09107-y

Airo, M.-L., & Loukola-Ruskeeniemi, K. (2004). Characterization of

sulfide deposits by airborne magnetic and gamma-ray responses in eastern Finland. *Ore Geology Reviews*, 24, 67–84. doi: **https://doi.org/10.1016/j.oregeorev.2003.08.008**

Alt-Epping, P., Diamond, L. W., & Wanner, C. (2022). Permeability and groundwater flow dynamics in

deep-reaching orogenic faults estimated from regional-scale hydraulic simulations. *Geochemistry, Geophysics, Geosystems*, 23(12), e2022GC010512. doi: **https://doi.org/10.1029/2022GC010512**

American Public Health Association, American Water Works Association, & Water Environment Federation. (2005). *Standard methods for the examination of water and wastewater*. American Public Health Association.

Andrés Sánchez, M. F., & Sánchez San Román, F. J. (1998). El sistema de flujo hidrotermal surgente en el Balneario de Ledesma (Salamanca). *Boletín Geológico y Minero*, 109(4), 391-400.

Armienta Hernández, M. A., & Rodríguez Castillo, R. (1995). Evaluación del Riesgo Ambiental Debido a la Presencia de Arsénico en Zimapán, Hidalgo. In *Memoria Final Fundación MAPFRE*. I.G.F., UNAM.

Armienta, M., Rodríguez, R., Aguayo, A., Ceniceros, N., Villaseñor, G., & Cruz, O. (1997a). Arsenic contamination of groundwater at Zimapan, Mexico. *Hydrogeology Journal*, 5, 39–46. doi: **https://doi.org/10.1007/s100400050111**

Armienta, M. A., Rodríguez, R., & Cruz, O. (1997b). Arsenic content in hair of people exposed to natural arsenic polluted groundwater at Zimapán, México. *Bulletin of Environmental Contamination and Toxicology*, 59, 583–589. doi: **https://doi.org/10.1007/s001289900519**

Armienta, M. A., & Segovia, N. (2008). Arsenic and fluoride in the groundwater of Mexico. *Environmental Geochemistry and Health*, 30(4), 345–353. doi: **https://doi.org/10.1007/s10653-008-9167-8**

Armienta, M., Villaseñor, G., Rodríguez, R., Ongley, L., & Mango, H. (2001). The role of arsenic-bearing rocks in groundwater pollution at zimapán valley, méxico. *Environmental Geology*, 40, 571–581. doi: **https://doi.org/10.1007/s002540000220**

Ayala, C., & Rey, C. (2009). Establecimiento de bases metodológicas para la obtención de cartografía gravimétrica 1: 50.000. aplicación a la modelización 2d y 3d en varias zonas de la península ibérica. *Ingeniería de Recursos Naturales y del Ambiente*, 12, 1-10.

Baranov, V., & Naudy, H. (1964). Numerical calculation of the formula of reduction to the magnetic pole.

Geophysics, 29(1), 67–79. doi: **https://doi.org/10.1190/1.1439334**

Camacho, M., & Alvarez, R. (2021). Geophysical modeling with satellite gravity data: Eigen-6c4 vs. ggm plus.

Engineering, 13(12), 690–706. doi: **https://doi.org/10.4236/eng.2021.1312050**

Carrillo-Martínez, M., & Suter, M. (1982). Tectónica de los alrededores de Zimapan, Hidalgo y Querétaro. In *Libro-guía de la excursión geológica de la región de Zimapán y áreas circundantes, Estados de Hidalgo y Querétaro*. Sociedad Geológica Mexicana.

Cebrian, M. E., Albores, A., Aguilar, M., & Blakely, E. (1983). Chronic arsenic poisoning in the north of Mexico.

Human Toxicology, 2(1), 121-133. doi: **https://doi.org/10.1177/096032718300200110**

Clark, I. (2015). *Groundwater geochemistry and isotopes*. CRC Press.

Comisión Nacional del Agua. (2021). *Límites de las cuencas hidrológicas de la República Mexicana* [Datos geoespaciales]. CONAGUA. **https://sigagis.conagua.gob.mx/aprovechamientos/fuente/pdf/Cuencas.pdf**

Corona-Esquivel, R., & Sanchez-Loyo, U. (2022). Reconocimiento geológico del área el espíritu, distrito minero de Zimapán, Estado de Hidalgo, México. (parte I). *Revista Geomimet*.

D'Amore, F., Scandiffio, G., & Panichi, C. (1983). Some observations on the chemical classification of ground waters. *Geothermics*, 12(2-3), 141-148. doi: **https://doi.org/10.1016/0375-6505(83)90024-X**

Del Razo, L. M., García-Vargas, G. G., Valenzuela, O. L., Castellanos, E. H., Sánchez-Peña, L. C., Currier, J. M., ... & Stýblo, M. (2011). Exposure to arsenic in drinking water is associated with increased prevalence of diabetes: a cross-sectional study in the Zimapán and Lagunera regions in Mexico. *Environmental Health*, 10(1), Art. 73. doi: **https://doi.org/10.1186/1476-069X-10-73**

Dentith, M., & Mudge, S. T. (2014). *Geophysics for the mineral exploration geoscientist*. Cambridge University Press.

Dove, P. M., & Rimstidt, J. D. (1985). The solubility and stability of scorodite, FeAsO4· 2H2O. *American Mineralogist*, 70(7-8), 838-844.

Eyankware, M. O., Ogwah, C., & Star, U. O. (2021). Integrated geophysical and hydrogeochemical characterization and assessment of groundwater studies in Adum West Area of Benue State, Nigeria. *Journal of Geological Research*, 3(3). doi: **https://doi.org/10.30564/jgr.v3i3.3197**

Fanton, G., Martínez, P., & Giménez, M. (2014). Procesamiento y analisis cualitativo de datos aeromagneticos con vistas a la exploración de yacimientos hidrotermales tipo lode gold-provincia de la rioja, argentina. *Geoacta*, 39(1), 30–50.

Fitz-Díaz, E., Tolson, G., Hudleston, P., Bolaños-Rodríguez, D., Ortega-Flores, B., & Vásquez Serrano, A. (2012). The role of folding in the development of the Mexican fold-and-thrust belt. *Geosphere*, 8(4), 931–949. doi: **https://doi.org/10.1130/GES00759.1**

Gómez-Hernández, A., Rodríguez, R., Del Río, A. L., Ruiz-Huerta, E. A., Armienta, M. A., Dávila-Harris, P., ... & Martínez-Villegas, N. (2020). Alluvial and gypsum karst geological transition favors spreading arsenic contamination in Matehuala, Mexico. *Science of the Total Environment*, 707, 135340. doi: **https://doi.org/10.1016/j.scitotenv.2019.135340**

González-Partida, E., Carrillo-Chávez, A., Levresse, G., Tritlla, J., & Camprubí, A. (2003). Genetic implications of fluid inclusions in skarn chimney ore, Las Animas Zn–Pb–Ag(–F) deposit, Zimapán, Mexico. *Ore Geology Reviews*, 23(1-4), 1-13. doi: **https://doi.org/10.1016/S0169-1368(03)00015-5**

Hanna Instruments Inc. (2020). *Manual de instrucciones HI 98196: Medidor multiparámetro portátil pH/ORP/DO/Presión/Temperatura*

[Manual]. Hanna Instruments Inc. **https://cdn.hannacolombia.com/hannacdn/support/manual/2020/09/Manual_HI_98196.pdf**

Hounslow, A. (2018). *Water quality data: analysis and interpretation*. CRC Press. doi: **https://doi.org/10.1201/9780203734117**

Hsu, S.-K., Sibuet, J.-C., & Shyu, C.-T. (1996). High-resolution detection of geologic boundaries from potential-field anomalies: An enhanced analytic signal technique. *Geophysics*, 61(2), 373–386. doi: **https://doi.org/10.1190/1.1443966**

Instituto Nacional de Estadística y Geografía. (2001). *Conjunto de datos vectoriales fisiográficos. Continuo Nacional. Escala 1:1 000 000. Serie I (Subprovincias fisiográficas)* [Datos geoespaciales]. INEGI.

Instituto Nacional de Estadística y Geografía. (2002). *Conjunto de datos vectoriales geológicos. Continuo Nacional. Fallas fracturas. Escala 1:1 000 000* [Datos geoespaciales]. INEGI.

Instituto Nacional de Estadística y Geografía. (2010). *Compendio de información geográfica municipal. Zimapán, Hidalgo* [Informe técnico]. INEGI. **https://www.inegi.org.mx/contenidos/app/mexicocifras/datos_geograficos/13/13084.pdf**

Ismail, E., Abdelhalim, A., Ali, A., Ahmed, M. S., Scholger, R., & Khalil, M. M. (2022). Isotopic, geophysical, and hydrogeochemical investigations of groundwater in west middle upper egypt. *ACS Omega*, 7(48), 44000–44011. doi: **https://doi.org/10.1021/acsomega.2c05387**

Jha, M., Kumar, S., Singh, T. B. N., Srivastava, S. K., Azad, G. K., & Yasmin, S. (2023). Potential health risk assessment through the consumption of arsenic-contaminated groundwater in parts of the middle Gangetic plain. *Bulletin of the National Research Centre*, 47, Art. 77. doi: **https://doi.org/10.1186/s42269-023-01054-5**

López, J. S. (2008). *Inventario físico de los recursos minerales del municipio Zimapán, Estado de Hidalgo*

[Informe]. Servicio Geológico Mexicano, Fideicomiso de Fomento Minero.

López-Loera, H., & Tristán-González, M. (2013). Geología y magnetometría aérea del graben de Villa de Reyes, San Luis potosí, mesa central de México: implicaciones tectónicas y geohidrológicas. *Boletín de la Sociedad Geológica Mexicana*, 65(1), 137–156. doi: **https://doi.org/10.18268/BSGM2013v65n1a11**

Martínez Flores, E. F., & Ortega Gamboa, V. (2009). *Estudio geológico económico del área Cerro Colorado, municipio de Zimapán, estado de Hidalgo, con apoyo de un sistema de información geográfica* [Tesis de licenciatura]. UNAM

Milligan, P., & Gunn, P. (1997). Enhancement and presentation of airborne geophysical data. *AGSO Journal of Australian Geology and Geophysics*, 17(2), 63–75.

Mora, J. C. (1998). *Estudio geológico minero evaluativo de lote ¨cerro colorado¨, municipio de Zimapán, Estado de Hidalgo* [Informe técnico]. Consejo de Recursos Minerales, Subdirección de Proyectos y Servicios, Distrito Minero de Zimapán.

Moreno Tovar, R., Téllez Hernández, J., & Monroy Fernández, M. G. (2012). Influencia de los minerales de los jales en la bioaccesibilidad de arsénico, plomo, zinc y cadmio en el distrito minero Zimapán, México. *Revista Internacional de Contaminación Ambiental*, 28(3), 203-218.

Morgan, L. A. (2012). *Geophysical characteristics of volcanogenic massive sulfide deposits* (Scientific Investigations Report 2010–5070–C, Chap. 7) [Informe de investigación científica]. U. S. Geological Survey. doi: **https://doi.org/10.3133/sir20105070C**

North American Magnetic Anomaly Group, Bankey, V., Cuevas, A., Daniels, D. L., Finn, C. A., Hernandez, I., Hill, P. L., Kucks, R., Miles, W., Pilkington, M., Roberts, C., Roest, W., Rystrom, V., Shearer, S., Snyder, S. L., Sweeney, R. E., & Velez, J. (2002). *Magnetic anomaly map of North America* (Geophysical Investigations Map GP–954) [Mapa]. U.S. Geological Survey. doi: **https://doi.org/10.3133/70211067**

Ramos Leal, J. A. (1996). *Parámetros estructurales que controlan la hidrodinámica de las aguas subterráneas en el área de Zimapán, Hgo.* [Tesis de maestría]. UNAM

Rankin, L. R., & Triggs, D. (1997). *Área de la Puna Argentina. Interpretación Geológica de Datos de Geofísica Aérea y Landsat TM* [Informe].

Ryan, W. B. F., Carbotte, S. M., Coplan, J. O., O'Hara, S., Melkonian, A., Arko, R., & Zemsky, R. (2009). Global multi-resolution topography synthesis. *Geochemistry, Geophysics, Geosystems*, 10(3), Q03014. doi: **https://doi.org/10.1029/2008GC002332**

Seequent. (2024, 10 de julio). *Oasis montaj 2024.1: Qué hay de nuevo* [Software de computadora]. Seequent. **https://www.seequent.com/es/oasis-montaj-2024-1-que-hay-de-nuevo/**

Secretaría de Salud. (1994). *Norma Oficial Mexicana NOM-014-SSA1-1993. Procedimientos sanitarios para el muestreo de agua para uso y consumo humano en sistemas de abastecimiento de agua públicos y privados* [Estándar]. Diario Oficial de la Federación. **https://salud.gob.mx/unidades/cdi/nom/014ssa13.html**

Secretaría de Salud. (2005). *Norma Oficial Mexicana NOM-230-SSA1-2002. Agua para uso y consumo humano, requisitos sanitarios que se deben cumplir en los sistemas de abastecimiento públicos y privados durante el manejo del agua. Procedimientos sanitarios para el muestreo* [Estándar]. Diario Oficial de la Federación. **https://www.dof.gob.mx/nota_detalle.php?codigo=2081772&fecha=12/07/2005#gsc.tab=0**

Secretaría de Salud. (2022). *Norma Oficial Mexicana NOM-127-SSA1-2021. Agua para uso y consumo humano.*

Límites permisibles de la calidad del agua [Estándar]. Diario Oficial de la Federación. **https://www.dof.gob.mx/nota_detalle_popup.php?codigo=5650705**

Servicio Geológico Mexicano. (2002). *Carta geológico-minera Tecozautla F14-C68: Hidalgo y Querétaro* (1.ª ed., escala 1:50 000) [Mapa]. Secretaría de Economía. **https://www.ingenieria.unam.mx/haaz/carpeta_de_material_de_haaz/geologia/mapas_de_geologia/mapa_geologico_tecozautla.pdf**

Shaji, E., Santosh, M., Sarath, K. V., Prakash, P., Deepchand, V., & Divya, B. V. (2021). Arsenic contamination of groundwater: A global

synopsis with focus on the Indian Peninsula. *Geoscience Frontiers*, 12(3), Art. 101079. doi: **https://doi.org/10.1016/j.gsf.2020.08.015**

Simons, F. S., & Mapes, E. (1956). *Geology and ore deposits of the Zimapán mining district, State of Hidalgo, Mexico* (No. 284) [Informe]. U.S. Geological Survey. **https://pubs.usgs.gov/pp/0284/report.pdf**

Singh, R., Gayen, A., Kumar, S., & Dewangan, R. (2021). Geo-spatial distribution of arsenic contamination of groundwater resources in intricate crystalline aquifer system of Central India: Arsenic toxicity manifestation and health risk assessment. *Human and Ecological Risk Assessment: An International Journal*, 27(6), 1588-1612. doi: **https://doi.org/10.1080/10807039.2020.1865787**

Song, K., Yang, G., Wang, F., Liu, J., & Liu, D. (2020). Application of geophysical and hydrogeochemical methods to the protection of drinking groundwater in karst regions. *International Journal of Environmental Research and Public Health*, 17(10), Art. 3627. doi: **https://doi.org/10.3390/ijerph17103627**

Sracek, O., Armienta, M. A., Rodríguez, R., & Villaseñor, G. (2010). Discrimination between diffuse and point sources of arsenic at zimapán, hidalgo state, mexico. *Journal of Environmental Monitoring*, 12(1), 329–337. doi: **https://doi.org/10.1039/B911873J**

Telford, W. M., Geldart, L. P., & Sheriff, R. E. (1990). *Applied geophysics*. Cambridge University Press.

Toushmalani, R. (2010). Application of gravity method in fault path detection. *Australian Journal of Basic and Applied Sciences*, 4(12), 6450–6460.

Vallée, M. A., Moussaoui, M., & Khan, K. (2024). Case studies of magnetic and electromagnetic techniques covering the last fifteen years. *Minerals*, 14(12), 1286. doi: **https://doi.org/10.3390/min14121286**

World Health Organization. (2011). *Guidelines for drinking-water quality* (4th ed.). WHO Press.